

Dynamic Nuclear Polarization of Selectively ^{29}Si -Enriched Core@shell Silica Nanoparticles

Jiwon Kim,^{††} Incheol Heo,^{††} Quy Son Luu,^{††} Quynh Thi Nguyen, Uyen Thi Do, Nicholas Whiting, Seung-Hyun Yang, Yong-Min Huh, Sun-Joon Min, Jeong Hyun Shim,^{*} Won Cheol Yoo,^{*} and Youngbok Lee^{*}



Cite This: *Anal. Chem.* 2023, 95, 907–916



Read Online

ACCESS |



Metrics & More

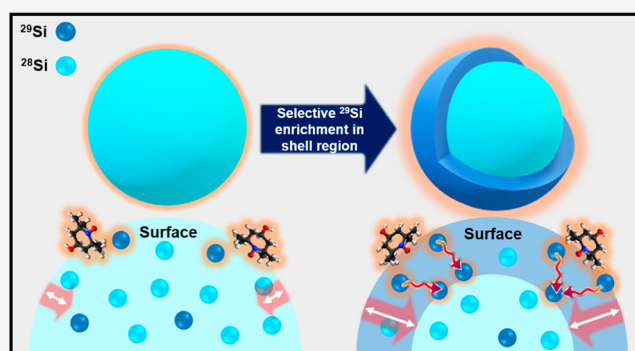


Article Recommendations



Supporting Information

ABSTRACT: ^{29}Si silica nanoparticles (SiO_2 NPs) are promising magnetic resonance imaging (MRI) probes that possess advantageous properties for in vivo applications, including suitable biocompatibility, tailorable properties, and high water dispersibility. Dynamic nuclear polarization (DNP) is used to enhance ^{29}Si MR signals via enhanced nuclear spin alignment; to date, there has been limited success employing DNP for SiO_2 NPs due to the lack of endogenous electronic defects that are required for the process. To create opportunities for SiO_2 -based ^{29}Si MRI probes, we synthesized variously featured SiO_2 NPs with selective ^{29}Si isotope enrichment on homogeneous and core@shell structures (shell thickness: 10 nm, core size: 40 nm), and identified the critical factors for optimal DNP signal enhancement as well as the effective hyperpolarization depth when using an exogenous radical. Based on the synthetic design, this critical factor is the proportion of ^{29}Si in the shell layer regardless of core enrichment. Furthermore, the effective depth of hyperpolarization is less than 10 nm between the surface and core, which demonstrates an approximately 40% elongated diffusion length for the shell-enriched NPs compared to the natural abundance NPs. This improved regulation of surface properties facilitates the development of isotopically enriched SiO_2 NPs as hyperpolarized contrast agents for in vivo MRI.



INTRODUCTION

Recent advances in magnetic resonance (MR) techniques provide high resolution, non-invasive soft tissue contrast without exposing patients to ionizing radiation. As such, magnetic resonance imaging (MRI) is a powerful diagnostic tool for providing three-dimensional anatomical imaging in humans.¹ Both MRI and magnetic resonance spectroscopy are extensively utilized in the clinic to detect changes in metabolic processes caused by various diseases and their corresponding treatments. However, because it is arduous to observe metabolites of intermediates and products with undetectable concentration level in MRI and magnetic resonance spectroscopy, it is challenging to obtain detailed mechanism about rapid biochemical reactions.^{2,3} Therefore, the development of a new technique that can provide critical insights regarding physio/pathological conversions at the cellular level is warranted. Similarly, research on tumor-targeted molecular imaging has recently been highlighted as an effective strategy for early-stage cancer diagnosis, which can identify disease locations using the specific binding of imaging probes.^{4–6} Multiple approaches have been proposed to increase the accumulation of contrast agents at tumor sites, including the modification of Gd^{3+} and the development of nanoplatform-

based targeting.^{7–12} However, these approaches lack a fundamental solution to overcome the inherent insensitivity of MR-based approaches. “Hyperpolarization” refers to a variety of techniques that temporarily enhance MR signals by several orders of magnitude through improved nuclear spin alignment and can be applied to low- γ nuclei such as ^{13}C , ^{15}N , and ^{29}Si to boost their MR sensitivity and aid in the development of targeted nanomaterial-based MR probes.^{13–20} Dynamic nuclear polarization (DNP) is a promising hyperpolarization technique, whereby high electron spin polarization is transferred to target nuclei via saturation of the spin resonance frequency of nearby electrons, typically at cryogenic temperatures and moderate magnetic field (e.g., >3 T). As interest in nanosystem-based molecular imaging probes has increased, the hyperpolarization of ^{29}Si nuclear spins in nanoparticles (NPs) using DNP has been demonstra-

Received: August 9, 2022

Accepted: December 6, 2022

Published: December 14, 2022



ted.^{17,21–30} Silicon NPs exhibit several advantageous characteristics that make the material well-suited to serve as an MR imaging probe, such as high biocompatibility, biodegradability, and long spin–lattice relaxation times at room temperature and in vivo.²¹ Moreover, endogenous electronic defects present in both the Si/SiO₂ surface interface and within the particle core are pivotal to generate a significant MR signal enhancement by providing electron spin sources to the DNP process.^{21,30} However, the practical implementation of silicon NPs as targeted MRI probes still have some functional difficulties, such as precise size control and distribution, low dispersibility in biological conditions, and uncontrolled surface modification. Overcoming these drawbacks will positively affect the stability, circulation time, and cellular uptake of NPs and allow them to serve as platforms for deep tissue MR imaging.^{31,32}

Silica NPs (SiO₂ NPs) possess several advantages compared to many other NPs, such as high biocompatibility, chemical inertness, water solubility, optical transparency, and ease of preparation. Additionally, they possess a smooth surface that is easily modified with functional moieties such as aptamers, peptides, or other specific receptors for effective tumor imaging.^{33,34} Despite this potential of SiO₂ NPs to serve as next-generation ²⁹Si MR imaging probes, few studies have been reported concerning DNP properties and ²⁹Si T₁ relaxation times for the particles, with the aim of future MRI implementation.^{35–37} One reason for this lack of preliminary results is due to the insufficient density of intrinsic electronic defects in SiO₂ NPs that can serve as an endogenous radical source for DNP. Silica can be locally polarized on its surfaces that directly contact exogenous radical species, leading to “surface-enhanced DNP-NMR” studies based on this feature.^{38–42} As such, chemical or physical modifications are needed to overcome the deficient SiO₂ DNP signal improvements that are due to the lack of requisite endogenous free electrons.³⁸

One approach to improve MR sensitivity of non-¹H spin systems include isotopic enrichment of the sample to increase the spin density of the MR-detectable isotope.²⁹ In this research, we selectively enriched the synthesized SiO₂ NPs in the ²⁹Si isotope, whereby the isotopic enrichment was either homogeneously enriched throughout the particle, or selectively enriched in the surface shell or particle core only. The goal was to effectively amplify ²⁹Si MR signals and examine the hyperpolarization characteristics of the particles in order to go overcome the DNP inefficiencies of silica NPs and maximize their potential as MRI probes. One aim of this work was to observe the effects of DNP efficiency by monitoring the ²⁹Si MR signal enhancement through selective isotope enrichment and to verify DNP polarization depth, which can monitor surface diffusion and spin exchange with extrinsic radicals. Here, core@shell SiO₂ NPs (40 nm core, 10 nm shell thickness) with selective ²⁹Si enrichments (4.7–35%) were prepared using a modified Stober method with an amino catalyst.⁴³ An important point of this investigation was to determine the influencing factors on signal sensitivity and T₁ relaxation time, which are critical MRI parameters; this was done by assessing the hyperpolarization attributes of SiO₂ particles that were selectively enriched with different ²⁹Si compositions. The measured DNP polarization depth provides key information on the diffusion behavior of spins from the surface of SiO₂ NPs to the core, which possesses few internal defects; this information suggests that methodical NP

modifications can be used to improve DNP and maximize ²⁹Si MR signals.

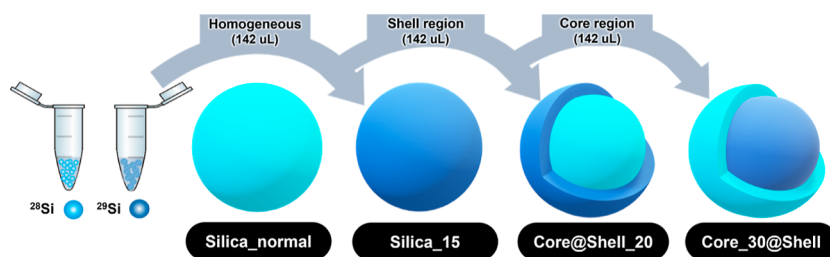
MATERIALS AND METHODS

Materials. ²⁸Si-TEOS was purchased from ACROS Organics (Geel, Belgium) and 100% ²⁹Si-TEOS was purchased from CortecNet (Les Ulis, France) as silicon precursors. L-Lysine (98%) was purchased from TCI (Japan, Tokyo). Anhydrous ethanol (Samchun Chemicals, Seoul, Republic of Korea) and 35% ammonium hydroxide solution (Sigma-Aldrich, MO, USA) were also used. Additionally, TEMPOL (4-hydroxy-2,2,6,6-tetramethylpiperidine-1-oxyl) solution needed for the DNP experiments was purchased from Sigma-Aldrich (MO, USA).

Synthesis of Core@Shell Silica NPs with Selective ²⁹Si Isotope Enrichment. SiO₂ NPs were synthesized using a modified Stober method with a two-step procedure. In the typical synthesis of the silica core, 4 mg of L-lysine was dissolved in 3.75 mL of deionized water while vigorously stirring and the mixture was heated to 90 °C. Then, 520 μL of TEOS was added to the solution and stirred for 24 h. Thereafter, for 10 nm shell fabrication, another 900 μL of TEOS was added into the mixture and the final reaction was allowed to proceed for 24 h while maintaining stirring and a constant temperature of 90 °C. The amount of 100% ²⁹Si-TEOS used for isotopic enrichment was calculated and added to the core and/or shell synthesis step(s) to adjust the ²⁹Si concentration. Typically, the same portion of 142 μL of 100% ²⁹Si-TEOS was used for enrichment of the 15% ²⁹Si abundance homogeneous silica (Silica_15), 30% ²⁹Si abundance core–normal shell (Core_30@Shell), and normal core–20% ²⁹Si abundance shell (Core@Shell_20) samples. Before adding to the reaction system, ²⁹Si-TEOS and ²⁸Si-TEOS were combined in an Eppendorf tube and mixed thoroughly with a vortex mixer. The final product was separated by centrifugation and the silica NPs were washed with ethanol (in between centrifuging) and were finally dried under vacuum at 100 °C.

Characterizations. The morphologies of the selectively ²⁹Si-enriched SiO₂ NPs were determined using scanning electron microscopy (SEM, Hitachi S4800, Japan) with an electron beam accelerated at 20 kV. For the SEM analysis, 0.5 mg/mL of each sample was dispersed in ethanol using probe sonication for 1 min at 70% amplitude (Vibra-Cell, VCX 130, 130 W, Sonics and Materials Inc., USA). Then, the suspension was dropped onto silicon chip substrates (SPI Supplies brand silicon chip substrate 5 × 5 mm × 525 μm thick). The average particle size and standard deviation were determined from SEM images by averaging the diameters of more than 100 particles using ImageJ (NIH, USA). Transmission electron microscopy (TEM) images were captured using a JEM-2100F microscope. For dynamic light scattering (DLS) measurements, the suspension was filtered through a polytetrafluoroethylene membrane 0.22 μm syringe filter. These residual suspensions were filled in a quartz cell (10 × 10 mm, Hellma Analytics, Germany) for hydrodynamic size measurements. This suspension was analyzed using a particle size analyzer (Anton Paar Litesizer 100, Austria) with a He–Ne laser (λ = 632.8 nm) at a back-scattered angle of 173°.

Solution-State and Solid-State ²⁹Si NMR Spectroscopy. For solution-state nuclear magnetic resonance (NMR) measurements, SiO₂ NP samples were leached using NaOH solution to confirm their core@shell structures. The leached

Scheme 1. Schematic Representation of the Four Main Samples in Which a Fixed Amount of ^{29}Si Nuclear Spin Isotope is Introduced to Each Site (Entire Particle, Only Shell, or Only Core) within the Particles^a

^aThe regions where ^{28}Si and ^{29}Si nuclear spins are dominant in each particle are expressed in light and dark blue, respectively.

samples were also analyzed with SEM to examine the leaching thickness and solution-state NMR was used for semi-quantitative determination of the proportion of ^{29}Si in each sample. A 1.5 mL Eppendorf tube was charged with 15 mg of either normal SiO_2 or selectively ^{29}Si -enriched silica samples—such as Core_30@Shell, Core@Shell_20, and Silica_15. Subsequently, 1 mL of NaOH (0.1 M) was added to the silica samples, after which the suspension was sonicated for 1 min using a bath sonication (Saehan Ultrasonication Co., SH-1050, South Korea, vibration frequency: 28 kHz, vibration output: 60 W). Subsequently, these samples were then shaken for 2 days at 27 °C using a LaboShaker D600 (Labogene, Korea). Finally, the supernatant and precipitant of each sample were collected using a microcentrifuge (Labogene mini, Labogene, Korea) at 12,000 rpm for 30 min. 250 μL of the supernatant solution was mixed with 28 μL D_2O (99% D, 0.05 wt % of 3-(trimethylsilyl)propionic-2,2,3,3- d_4 acid, sodium salt), and this mixture was added to a Teflon NMR tube (OD 3.75 mm). In addition to the NMR analysis, to determine the leached shell thickness of the particles, the precipitant was re-dispersed in deionized water and SEM analysis was performed to measure the leached shell thickness. The solution-state ^{29}Si NMR spectra of each sample were acquired at 298 K using a 400 MHz NMR spectrometer equipped with a broadband probe containing pulsed field gradients (Bruker Biospin, Billerica, MA, USA). Furthermore, solid-state NMR (SS-NMR) measurements were primarily conducted to compare and analyze the chemical structure of the particles and confirm whether structural changes occurred depending on the isotopic enrichment. For structural comparison of the particles, 1D ^{29}Si MAS spectra were measured using a high-power decoupling (HPDEC) pulse sequence on the same NMR spectrometer at a spinning rate of 10 kHz. To estimate the surface features of the particles, ^{29}Si cross-polarization/magic-angle spinning (CP/MAS) NMR spectra were recorded at a spinning speed of approximately 10 kHz.

DNP System and Experiments. The laboratory-constructed DNP system consists of a continuous flow He cryostat (Oxford, 3.3 K), a superconducting magnet (Oxford, 5 T), a microwave source (Virginia Diode, 139–141 GHz, 500 mW), and a cryogenic DNP insert. The output power of the microwave source was \sim 500 mW, which was calibrated using a power meter (Erickson PM5). The microwave diode was positioned external to the cryostat, and the generated microwaves were guided to silicon particles within the DNP insert through a D-band waveguide. The end of the waveguide was bent at a right angle to the sample region and was terminated by an open-type antenna (QuinStar, customized model), which launched the microwave to the sample. A saddle

coil surrounding the sample and two variable capacitors were used to construct a ^{29}Si NMR probe head. The extent of DNP enhancement was measured using this in situ ^{29}Si NMR. A temperature sensor (Cernox, Lakeshore) was mounted near the sample region. By reducing helium pressure inside the cryostat, the sample temperature was lowered to \sim 3.3 K, as monitored by the sensor. The cryostat has a sample port on the top, through which hyperpolarized samples can be ejected into the room temperature lab space. The cryogenic DNP insert has a hollow middle structure, which holds a carbon pipe used for manual sample ejection. To avoid encountering any zero-field regions during the ejection, guiding coils and ring magnets are installed near the sample exit port of the DNP insert. On top of the exit port, there is a magnetic carrier constructed of a Halbach array magnet, with a central field of \sim 0.3 T, to mitigate T_1 losses during sample transport following DNP. Silica particle samples were prepared inside a DNP sample tube. The NMR tube was mounted at the bottom of the carbon pipe and then loaded into the microwave-active region of the cryostat; cooling the cryostat to 3.3 K typically required \sim 2 h. The optimal microwave frequency for ^{29}Si DNP was selected from a sweep test (Figure S5 in Supporting Information). The maximum ^{29}Si NMR peaks were found at 140 GHz, which is consistent to previous reports on silicon NPs.²⁹ During DNP, the sample temperature was maintained at 3.3 K, and the microwave was irradiated at 140 GHz with the max power of 500 mW. The enhanced ^{29}Si MR signal was monitored with a small flip angle (10°) pulse and 6 min delay between pulses. To obtain the max ^{29}Si polarization, the DNP time was extended up to 1 h. After that, the microwave was turned off and a polarization decay test was used to measure the T_1 relaxation using a 4 min delay and 10° pulses for 1 h.

RESULTS AND DISCUSSION

In order to determine the optimal ^{29}Si isotopic enrichment approach to the SiO_2 NP structures, the specific locations of enrichment were selectively controlled within the homogeneous and core@shell silica NPs by using the same amount of ^{29}Si enrichment precursor in each case. This allowed the DNP signal enhancement level and polarization depth approximation to be performed more proficiently with respect to the scheme of applying the same amount of ^{29}Si isotope to a specific area inside the particle (Scheme 1).

In this study, the size of the homogeneous and core@shell SiO_2 NPs was fixed at 60 nm in diameter whereas the shell thickness was maintained at 10 nm for the core@shell SiO_2 NPs. Given that the conventional Stober method has difficulty in effectively producing monodisperse SiO_2 NPs smaller than 100 nm, we successfully synthesized highly monodisperse SiO_2

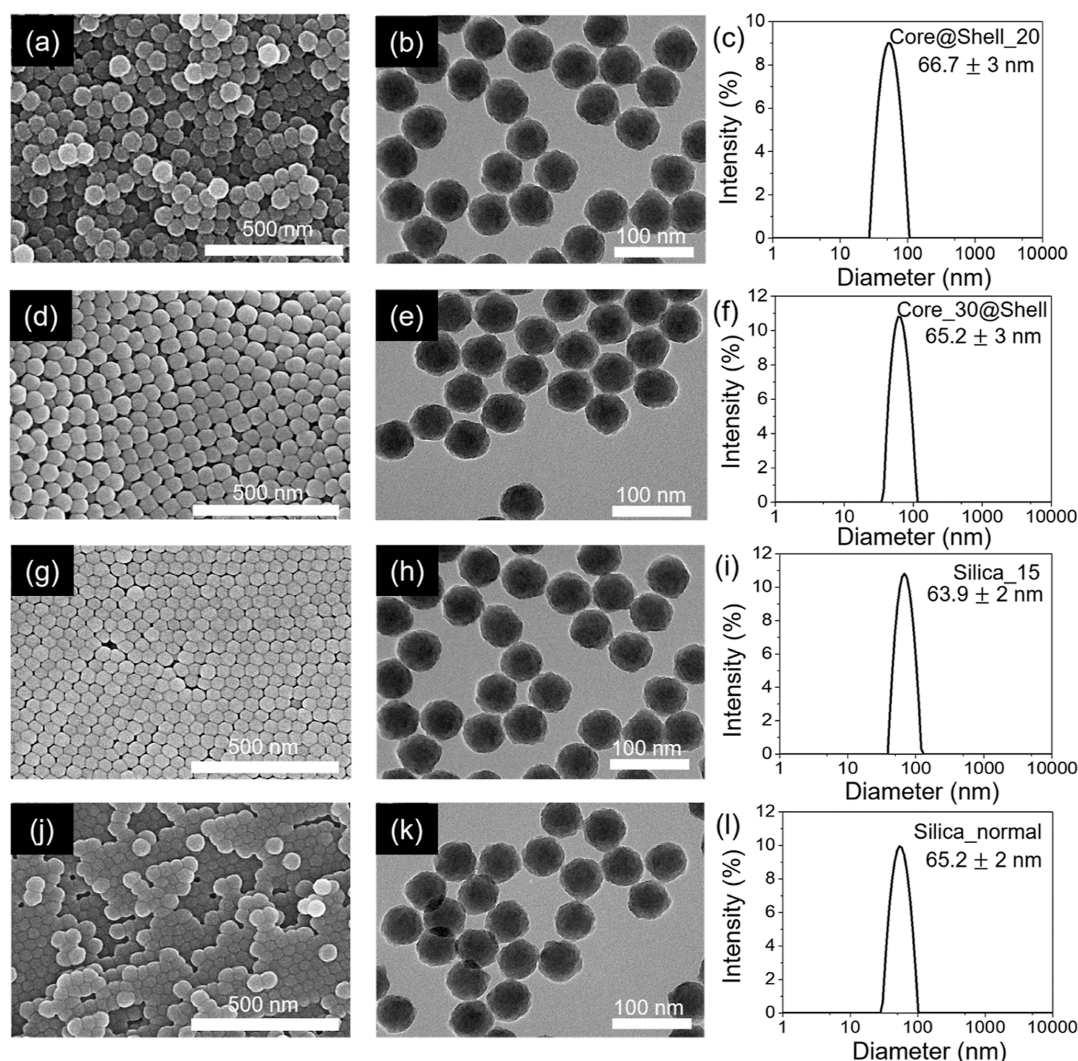


Figure 1. Representative SEM and TEM images, and DLS results of the 60 nm diameter selectively ^{29}Si enriched SiO_2 NPs. The above data were measured following the shell formation and showed the final morphology of the particles. The corresponding result for a core seed with a size of 40 nm are confirmed in the Supporting Information. Each row exhibits a narrow size distribution and spherical shape for Core@Shell_20 (a–c), Core_30@Shell (d–f), Silica_15 (g–i), and Silica_normal (j–l).

NPs via a modified Stober approach that utilized L-lysine as the base catalyst and surfactant.^{44,45} For the core@shell SiO_2 NPs, a seeded growth method was utilized to control the location of ^{29}Si enrichment. For example, SiO_2 NPs can be produced to have a 40 nm core consisting of natural abundance ^{29}Si (4.7%); this can then be enveloped with a 10 nm shell that contains isotopically enriched ^{29}Si (20%), denoted here as Core@Shell_20. Similarly, the 40 nm silica cores that were synthesized with ^{29}Si enriched to 30%, then enveloped with a natural abundance ^{29}Si shell of 10 nm, were denoted as Core_30@Shell. Furthermore, we also synthesized 60 nm SiO_2 NPs by the seeded growth method with a homogeneous distribution of 15% ^{29}Si isotopic enrichment, denoted as Silica_15. Lastly, 60 nm silica NPs produced using only the natural abundance ^{29}Si silica precursor were denoted as Silica_normal. According to the SEM and TEM images shown in Figure 1a,b,d,e, highly monodispersed Core@Shell_20 and Core_30@Shell silica NPs with 63.3 ± 2 and 62.8 ± 1 nm, respectively, were successfully produced, confirming the 10 nm shell thickness. In addition, DLS measurements determined that the size distributions of the

Core@Shell_20 and Core_30@Shell samples were 66.7 ± 3 and 65.2 ± 3 nm, respectively (Figure 1c,f); this was similar to the SEM and TEM investigations, and confirms the monodispersity of the samples. Lastly, the sizes of the Silica_15 and Silica_normal samples were measured as 62.8 ± 2 and 62.8 ± 2 nm, respectively (Figure 1g,h,i,k), confirmed by DLS (Figure 1i,l).

Characterization of the isotopically enriched SiO_2 NPs enabled a deeper understanding of the morphology and particle size of the materials. Additionally, the internal structures of the different NP types were compared using ^{29}Si SS-NMR. The ^{29}Si HPDEC/MAS spectra shown in Figure 2 contain a predominant signal at -107 ppm that corresponds to the chemical shift of $(\text{Si}-\text{O})_4\text{Si}$ (Q_4) and a shoulder signal at -97 ppm represents the chemical shift of $(\text{Si}-\text{O})_3\text{Si}(\text{OH})$ (Q_3).⁴⁶ The molecular structures of these NPs were characterized using the ratio between the Q_4 and Q_3 bands, where a Gaussian deconvolution fitting was applied (OriginLab Corporation, MA, USA). As displayed in Figure 2a–d, all particle types exhibited comparable Q_4/Q_3 ratios regardless of the selective ^{29}Si isotope enrichment, exhibiting comparable

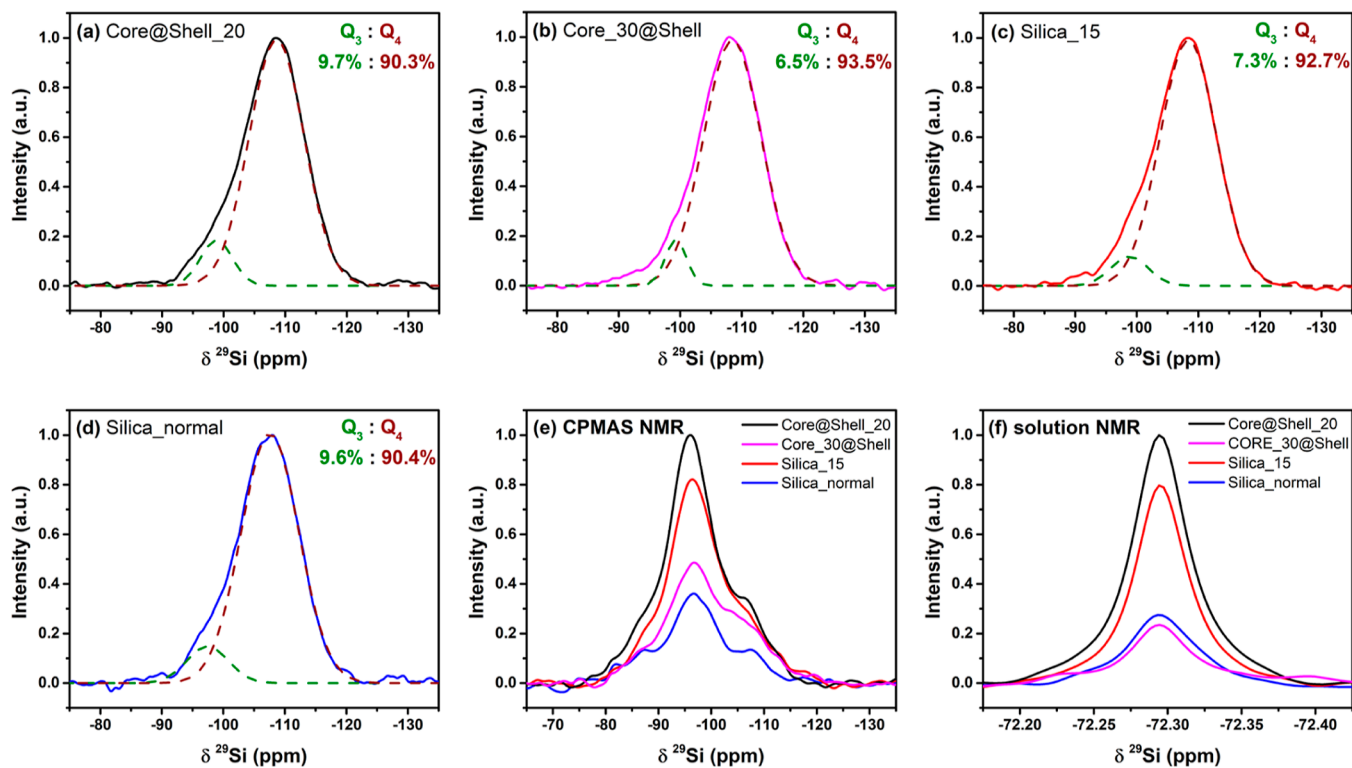


Figure 2. (a–d) Normalized ^{29}Si HPDEC/MAS NMR spectra, (e) ^{29}Si CP/MAS NMR spectra, and (f) ^{29}Si liquid NMR spectra of the etched silicates from the leached samples. All experiments were conducted with 400 MHz (9.4 T) SS-NMR at room temperature.

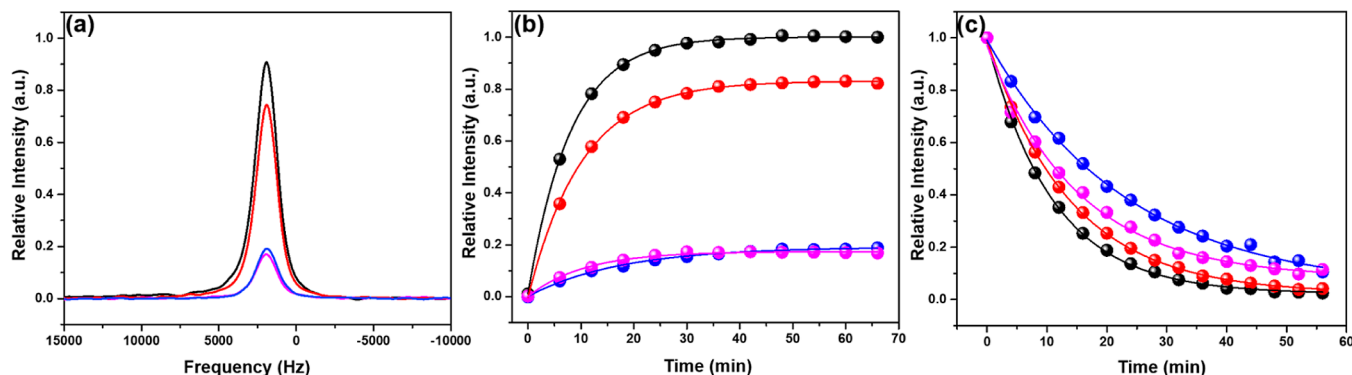


Figure 3. DNP signals of Silica_15 (red), Core@Shell_20 (black), Core_30@Shell (pink), and Silica_normal (blue) samples. (a) Hyperpolarized ^{29}Si MR spectra obtained by a single 90° of single pulse after 1 h of DNP. (b) Buildup of the hyperpolarized ^{29}Si MR signal over time. Each sample (~ 60 mg of the enriched SiO_2 NPs with 50 mM TEMPOL solution) was hyperpolarized using DNP, and the data were measured every 6 min with a 10° of small flip angle pulse. (c) Signal decay of hyperpolarized ^{29}Si MR at cryogenic temperature. A spectrum was acquired every 4 min over a period of 60 min and through a series of 10° flip angle excitations. All DNP experiments were performed at 5 T magnetic field while maintaining a sample temperature of 3.3 K.

molecular structures. From the ^{29}Si SS-NMR spectra, Q_4 was the dominant band for all samples. This follows from the use of calcination during synthetic synthesis to remove the lysine catalyst from the particles; at high temperatures, hydroxyl groups on the particle surface and/or core can also be eliminated due to simultaneous condensation. Surface-specific features of these particles were also analyzed by ^{29}Si CP/MAS NMR (Figure 2e). The ^{29}Si CP/MAS NMR spectra showed different Q-types of silicon positions (Q_4 – Q_2), which were detected at approximately -106 , -97 , and -87 ppm, respectively.⁴⁶ Because surface-specific silicon sites (Q_3 , Q_2) are expected to be preferentially detected using cross-polarization, the Q_3 silicon site was the dominant peak in all

CP spectra. All particle types except the Core_30@Shell exhibited similar Q_4/Q_3 ratios regardless of the selective ^{29}Si isotope enrichment and exhibited similar surface environments. Because of the selective core enrichment (Q_4 specific site) in the Core_30@Shell sample, the area of the Q_4 band was slightly higher than that of the other particle types. Furthermore, to verify the quantitative selective enrichments of the particles, we conducted ^{29}Si solution-state NMR measurements after having etched the particles with NaOH solution. After 2 days of incubation in the etching solution, an average of 6 nm of particles' shells were effectively leached and degraded into a small molecule silicate, H_3SiO_4^- . The thickness of the etched layer was determined by SEM (Supporting Informa-

tion), and the concentration of the silicate species within the etched layer was determined by intensity of the NMR peak at -72.3 ppm.^{47,48} As can be seen in Figure 2f, both Core@Shell_20 and Silica_15 showed approximately fourfold and threefold higher intensities than the naturally abundant sample (Silica_normal), respectively, indicating a linear concentration relationship of the selective enrichments in the shell layer. However, Core_30@Shell particles exhibited the same tendency as the Silica_normal because their local spin concentrations on the etched layer were synthetically identical (i.e., natural abundance). The observation verifies the accurate design of the selective ^{29}Si isotopic enrichments on different types of core@shell and homogeneous structures.

Through physical and chemical characterization of ^{29}Si -enriched core@shell SiO_2 NPs, including both Silica_15 and Silica_normal NPs, morphological information and quantitative verification of ^{29}Si ratios in the particles could be determined. Subsequently, low-temperature DNP experiments were conducted to demonstrate that the SiO_2 NPs can be used as effective MRI probes. During DNP, 60 mg of the SiO_2 NPs were mixed into TEMPOL solutions of either 50 or 30 mM (Supporting Information) to provide exogenous electrons for ^{29}Si DNP. A short sample tube containing the NPs suspended in TEMPOL was polarized at 3.3 K after being manually inserted into the lab-constructed DNP instrument using a carbon pipe. Microwave-dependent polarization enhancements of the ^{29}Si spins in the particles were tested (Supporting Information), and the optimal microwave frequency of 140.0 GHz was irradiated at the sample for 1 h. Time constants of the buildup and decay of hyperpolarized ^{29}Si signal were measured in situ using the onboard NMR circuit, which allowed quantitation of the DNP signal improvement and subsequent T_1 rate following DNP. The buildup of ^{29}Si MR signal was monitored every 6 min for 1 h using 10° pulses; the time constant of this buildup was calculated using a single exponential fit of the data (Figure 3b). Representative hyperpolarized ^{29}Si MR spectra of the samples were acquired with a $\pi/2$ pulse after 1 h of polarization to compare the DNP enhancements between the selective isotope enrichment categories. Because all of the selectively ^{29}Si -enriched samples (Core@Shell_20, Core_30@Shell, and Silica_15) were synthesized by utilizing the same number of ^{29}Si nuclear spins, similar DNP features would be expected between the samples. As shown in Figure 3a, Core@Shell_20 and Silica_15 NPs showed 5.5 and 4.5 times higher signal improvements over the intensity of Core_30@Shell and Silica_normal NPs. These results demonstrate that the extent of nuclear spin polarization increases with ^{29}Si enrichment ratios on the particles' surface only, resulting in a linear dependence. According to previous reports, silicon NPs showed non-linear improvement to ^{29}Si MR signals due to changes in internal defects and excessively augmented spin diffusion.²⁸ The results presented here indicate that the majority of the hyperpolarization process is confined to the particles' shells, and that spin diffusion does not carry the increased polarization deep into the particle core. This behavior is also observed in polarization build-up curves (Figure 3b), in which the Core@Shell_20 sample possesses a relatively fast build-up time constant (8.0 min), while the build-up constant is lengthened as the amount of the ^{29}Si enrichment in the surface layer is diminished (Silica_15: 10.2 min; Core_30@Shell: 10.5 min; Silica_normal: 17.6 min). In the cases of Core@Shell_20 and Silica_15 samples, there are more ^{29}Si spins in the NP's surface

that are in close proximity with exogenous TEMPOL radicals; these ^{29}Si spins are quickly polarized, and the enhanced magnetization can then be efficiently transferred throughout the shell via spin diffusion. Interestingly, the build-up curve of the Core_30@Shell sample produced a relatively similar time constant as the shell-enriched samples (Core@Shell_20 and Silica_15), even though the particle core is enveloped by a shell layer that is naturally abundant in ^{29}Si . This could be potentially explained by a condensed ^{29}Si spin pool in the 30% enriched core that might induce faster diffusions to the surface spins. However, the Core_30@Shell sample displays a qualitatively similar buildup curve to the Silica_normal sample (Figure 3b).

Along with the polarization build-up experiments, the signal decay of enhanced ^{29}Si magnetization was monitored at cryogenic temperatures for each sample (Figure 3c). Following a set polarization time of 1 h, a 10° pulse was applied to the sample every 4 min to determine the T_1 using in situ ^{29}Si NMR. Similar to the build-up time constants, the T_1 results verify that samples with higher ^{29}Si enrichment in the shells experienced faster T_1 relaxation times, which shows that the ^{29}Si ratio of the shell has a great influence on the lifetime of the signal. This dependence is likely due to the dipole–dipole interaction that occurs predominantly in the shell layer of the SiO_2 NPs, where the exposure of surface ^{29}Si spins to exogenous radicals is crucial. Specifically, the Core_30@Shell sample experienced a relaxation time that was 1.5 \times faster than the Silica_normal sample, which parallels the trend in build-up time constant during DNP. Although a detailed study is needed to fully explain this outcome, it is plausible that the density of ^{29}Si nuclei in the core has an authoritative influence on the depolarization process of the shell layer rather than the core polarization itself. Decay of the hyperpolarized ^{29}Si MR signal is much faster as the ratio of isotopic enrichment increases, as spin–spin relaxation is a major contributor for faster T_1 . Therefore, an optimal dilution of ^{29}Si is needed to achieve a balance between high ^{29}Si MR signal intensity and long T_1 .

After affirming the primary hyperpolarization characteristics for the four different particle types, additional selectively ^{29}Si -enriched SiO_2 NPs with different ^{29}Si ratios were prepared and tested in DNP experiments to verify the previous results (Core@Shell_35, Core@Shell_15, and Core_15@Shell; Supporting Information). Similar to the first group of particle types, the Core@Shell_35 sample achieved approximately 10 \times higher ^{29}Si MR signals compared to the Silica_normal and Core-only enriched NPs. Additionally, both the homogeneously ^{29}Si -enriched (15%) sample (Silica_15) and Core@Shell_15 sample displayed comparable ^{29}Si signal intensities despite their different isotope enrichments in the core. This result indicates that the region where hyperpolarization has its greatest effect in these particles is less than 10 nm from the surface, demonstrating that the ratio of ^{29}Si present in the particle shell is a compelling factor for improved ^{29}Si MR signal intensity. In order to more precisely investigate the effects of ^{29}Si isotope enrichment on signal enhancement, we estimated the DNP polarization depth using a model. For simplicity, we adopted a hard-shell model, in which ^{29}Si polarization is spatially uniform. First, we assumed a 5.7 nm polarization depth for the 60 nm of Silica_normal NPs;⁴⁶ these NPs have a natural abundance of ^{29}Si spins (4.7%) and are used to normalize the rest of the data. The number of ^{29}Si nuclei in the

Table 1. Summary of Hyperpolarization Features of All SiO₂ NPs

samples	polarization ratio ϵ^a	estimated signal enhancement ϵ_{Si}	T_r build-up (min) ^b	T_1 (min) ^c	a (nm) ^d	estimated number of unit cell polarized ^e	estimated number of ²⁹ Si nuclei polarized ^f
Silica_normal	1.00	26	17.7	25.5	5.7 ^{ref}	54×10^2	55×10^3
Core@Shell_15	4.37	11×10^1	11.6	15.8	8.7	74×10^2	24×10^4
Core@Shell_20	5.50	16×10^1	8.0	11.6	8.0	70×10^2	30×10^4
Core@Shell_35	9.90	25×10^1	6.0	5.7	8.3	72×10^2	54×10^4
Core_15@Shell	1.14	29	16.6	23.4	6.7	62×10^2	63×10^3
Core_30@Shell	0.95	22	10.6	16.1	5.3	51×10^2	52×10^3
Silica_15	4.54	98	10.2	14.6	9.2	77×10^2	25×10^4

^aRatio of the enhancement factor relative to the Silica_normal sample. ^bBuild-up constant time was calculated by fitting a mono-exponential fitting of the build-up data. ^cSpin–lattice relaxation time of each sample. ^dDNP polarization depth of each sample on assumption that the penetration depth of Silica_normal is 5.7 nm. ^eEstimated number of unit cell that was polarized. ^fEstimated number of ²⁹Si polarized nuclei.

polarized region of this sample (5.7 nm from the surface) can be calculated using eq 1

$$N_{\text{polarized } ^{29}\text{Si}} = \frac{\frac{4}{3}\pi r^3 - \frac{4}{3}\pi(r-a)^3}{d^3} \times 216 \times f \quad (1)$$

where r is the radius of the SiO₂ NPs (nm), a is the DNP polarization depth (nm), $d = 2.139$ nm is the lattice constant of amorphous SiO₂, 216 is the number of Si atoms in an amorphous SiO₂ unit cell (Supporting Information), and f is the ²⁹Si isotope abundance (as a percentage) in the polarized region. Based on the ratio of enhanced ²⁹Si MR signals between the enriched samples and Silica_normal sample, the number of polarized ²⁹Si nuclei for each enriched particle was calculated. From this, the DNP polarization depths of the enriched SiO₂ samples were then determined using the information from eq 1; these estimations along with other DNP characteristics are available in Table 1 (also, Supporting Information).

From these calculations, the polarization depths of Silica_15 and Core@Shell_15 were 9.2 and 8.7 nm, respectively; the ²⁹Si isotope abundance for both of these samples was 15%. Along with similar ²⁹Si spin density in the polarized region and polarization depth, both samples experienced similar ²⁹Si MR enhancement factors. Comparing the Core_15@Shell, Core_30@Shell, and Silica_normal samples, which all contained natural abundance ²⁹Si in the shell region, resulted in a calculated polarization depths that ranged from 5.3 to 6.7 nm stemming from the different samples (which also shared relatively similar ²⁹Si MR enhancement values). With regard to Core@Shell_20 and Core@Shell_35 samples: although their estimated polarization depth from model calculation was slightly less than for the Core@Shell_15 and Silica_15 samples, they still provided the highest enhancement factors among all investigated samples due to the high density of ²⁹Si nuclei in the shells of these samples. Samples with varying ²⁹Si isotopic enrichment in only their shell layers have DNP polarization depths that are comparable to Silica_normal, which provides an opportunity to revisit the spin diffusion model. The spin diffusion constant (D) is often given as the approximate relation: $D \cong b^2/50T_2$, where b denotes the distance between ²⁹Si nuclei and T_2 is spin–spin relaxation time.²⁰ Theoretical aspects of the linewidth of MR peaks from crystalline NPs consisting of homogeneously distributed spins are expected to display linear and square-root dependences when $f < 10\%$ and $f > 50\%$, respectively. However, these experiments produced hyperpolarized spectra with linewidths of approximately 1500 Hz full width at half-maximum, which is inconsistent with the contribution from dipole–dipole

interactions only. In the work presented here, it is likely that the major line broadening effect is dominated by paramagnetic relaxation due to the proximity of the exogenous radical to the surface of SiO₂ NPs. Moreover, determination of the true line broadening of the samples due to isotope enrichment is hindered by the amorphous features of the SiO₂ NPs and inherent inhomogeneity of B_0 in the DNP device; this limits our ability to indirectly determine the spin diffusion constant from T_2 when dipolar interactions are not the dominative source of line broadening. This was partially addressed by lowering the radical concentration to 30 mM of TEMPOL, which resulted in linewidths that were $\sim 10\%$ narrower compared to using 50 mM TEMPOL. However, even these results did not match well with theoretical expectations. Simulations exhibited a linear dependency between the spin diffusion constant and isotopic enrichment but provided smaller polarization depth values; this can potentially be explained by relatively inefficient spin diffusion that is caused by an extended amorphous ²⁹Si–O network (as opposed to a condensed and crystalline ²⁹Si–²⁹Si network). Because of this discrepancy, a more elaborate model is currently under development to rigorously explain the effect of the ²⁹Si isotopic enrichment on spin diffusion in SiO₂ NPs.

Besides, 1D ²⁹Si hyperpolarization spectra were recorded with or without microwave irradiation to verify signal improvements obtained by DNP. Subsequently, we compared the integrated signal intensity of hyperpolarized samples with the thermal equilibrium signal to determine DNP enhancement value of ²⁹Si (ϵ_{Si}) in the solid state. The direct DNP in ²⁹Si nuclei remarkably improved the signal intensity of silica samples (see Figure S9). In particular, DNP enhancement factors ϵ_{Si} of 98, 16×10^1 , 22, and 26 were achieved from Silica_15, Core@Shell_20, Core_30@Shell, and Silica_normal particles, respectively. The estimated signal enhancement for each sample showed a similar trend as the polarization ratio compared in the previous section. In other words, it can be confirmed that ²⁹Si isotope enrichment for the shell region of the particle is an effective method to induce a boost in signal intensity. Samples that were selectively enriched in the shell region (Core@Shell_15, Core@Shell_20, Core@Shell_35) showed higher signal improvements compared to samples with core-specific enrichments (Core_15@Shell, Core_30@Shell), and it was also corroborated that the enhancement factors ϵ_{Si} increased as the ²⁹Si ratio increased. Moreover, Core@Shell_20, which presented a value about 20% greater than that of Silica_15 in the polarization ratio, exhibited a 60% higher aspect than the Silica_15 sample in DNP enhancement. From the evidence above, increasing ²⁹Si spin density in the

particle shell region is an advantageous approach to develop high-resolution MRI probes with improved signal amplifications.

These hyperpolarization studies on selective ^{29}Si isotopic enrichment of SiO_2 NPs are the first to demonstrate the potential for ^{29}Si MR imaging and provide structural information for ^{29}Si isotope enrichment in SiO_2 NPs. Taking advantage of core@shell NP designs allowed valuable knowledge about the efficiency of ^{29}Si isotope enrichment and polarization depths into the SiO_2 NPs to be obtained. Although both the initial level of hyperpolarization and the effective polarization depth are generally greater for the shell-enriched SiO_2 NPs, the relaxation decay is also much faster because of dipole–dipole interactions and faster diffusion. Due to instrumentation limitations, it was challenging to directly measure the signal decay of the hyperpolarized ^{29}Si MR signal at room temperature for the sample treated in this study, but we measured ^{29}Si spin–lattice relaxation time of the Core@Shell_20 sample under thermal equilibrium conditions using solid-state magic-angle spinning NMR to explore T_1 relaxation trend of ^{29}Si -enriched SiO_2 NPs. The T_1 (at thermal equilibrium) of this sample was determined at ~ 20 s (see Figure S10), which is judged to be remarkably short for immediate biomedical application. In succession to the present work, we are working to extend ^{29}Si T_1 in silica particles by adjusting the synthesis path of samples to optimize physicochemical properties such as crystallinity. Furthermore, we have fabricated silica particles that have radicals (e.g., TEMPOL) embedded throughout in order to maximize the DNP efficiency of the NPs. The fabrication of SiO_2 NPs with selectively ^{29}Si -enriched core–shell structures described in this work is the foundation of a multi-stage project, as we continue to apply DNP to silica particles in order to determine their potential for future clinical implementation.

CONCLUSIONS

We have demonstrated a straightforward method of synthesizing selectively ^{29}Si -enriched homogeneous and core@shell SiO_2 NPs with a high level of control in terms of the materials' size, morphology, and internal structure. ^{29}Si hyperpolarization characteristics of the different NP types, ranging from the nuclear spin enhancement factor and build-up time constant to the depolarization rate at cryogenic temperature were determined. In summary, larger signal amplifications were observed as the ^{29}Si ratio of the particle shell increased, regardless of substantial enrichments in the particle core. Despite high ^{29}Si isotopic enrichment in the particle core, the overall polarization level is equivalent to the naturally abundant samples due to the shallowness of the effective polarization depth. The shell-enriched samples (Core@Shell_15, Core@Shell_20, and Core@Shell_35) achieved higher ^{29}Si polarization levels, with similar polarization depths. These developments are part of an integrated strategy to utilize the bioinspired SiO_2 NPs as MRI probes in the future. Furthermore, DNP-NMR with core@shell NPs is expected to allow for the fast characterization of surface-attached moieties, providing precise knowledge of the surface composition and chemistry of SiO_2 NPs, including biochemical interactions with substrates.

ASSOCIATED CONTENT

Supporting Information

The Supporting Information is available free of charge at <https://pubs.acs.org/doi/10.1021/acs.analchem.2c03464>.

Experimental procedures, SEM images, TEM images, ^{29}Si SS-NMR spectra, sweep test, and DLS analysis (PDF)

AUTHOR INFORMATION

Corresponding Authors

Jeong Hyun Shim – Quantum Magnetic Imaging Team, Korea Research Institute of Standards and Science, Daejeon 34113, South Korea; Department of Applied Measurement Science, University of Science and Technology, Daejeon 34113, South Korea; Email: jhshim@kriss.re.kr

Won Cheol Yoo – Department of Applied Chemistry, and Department of Chemical and Molecular Engineering, Center for Bionano Intelligence Education and Research, Hanyang University, Ansan 15588, South Korea; orcid.org/0000-0002-4450-9744; Email: wcyoo@hanyang.ac.kr

Youngbok Lee – Department of Applied Chemistry, and Department of Chemical and Molecular Engineering, Center for Bionano Intelligence Education and Research, Hanyang University, Ansan 15588, South Korea; orcid.org/0000-0002-8392-0827; Phone: +82 31 400 5500; Email: yblee@hanyang.ac.kr

Authors

Jiwon Kim – Department of Bionano Technology, Center for Bionano Intelligence Education and Research, Hanyang University, Ansan 15588, South Korea

Incheol Heo – Department of Applied Chemistry, and Department of Chemical and Molecular Engineering, Center for Bionano Intelligence Education and Research, Hanyang University, Ansan 15588, South Korea

Quy Son Luu – Department of Bionano Technology, Center for Bionano Intelligence Education and Research, Hanyang University, Ansan 15588, South Korea

Quynh Thi Nguyen – Department of Applied Chemistry, and Department of Chemical and Molecular Engineering, Center for Bionano Intelligence Education and Research, Hanyang University, Ansan 15588, South Korea

Uyen Thi Do – Department of Bionano Technology, Center for Bionano Intelligence Education and Research, Hanyang University, Ansan 15588, South Korea

Nicholas Whiting – Department of Physics & Astronomy and Department of Biological & Biomedical Sciences, Rowan University, Glassboro, New Jersey 08028, United States; orcid.org/0000-0003-2306-4982

Seung-Hyun Yang – Department of Radiology, College of Medicine and Interdisciplinary Program in Nanomedical Science and Technology, Nanomedical National Core Research Center, Yonsei University, Seoul 03722, South Korea

Yong-Min Huh – Department of Radiology, College of Medicine, Severance Biomedical Science Institute, College of Medicine, YUHS-KRIBB Medical Convergence Research Institute, College of Medicine, and Department of Biochemistry & Molecular Biology, College of Medicine, Yonsei University, Seoul 03722, South Korea

Sun-Joon Min – Department of Applied Chemistry, and Department of Chemical and Molecular Engineering, Center

for Bionano Intelligence Education and Research, Hanyang University, Ansan 15588, South Korea; orcid.org/0000-0003-0867-4416

Complete contact information is available at:

<https://pubs.acs.org/10.1021/acs.analchem.2c03464>

Author Contributions

^{††}J.K., I.H., and Q.S.L. contributed equally to this work.

Notes

The authors declare no competing financial interest.

ACKNOWLEDGMENTS

This research was supported by the National Research Foundation of Korea (NRF-2020R1A4A4079870 and NRF-2022R1A2C4001273), GRRC program of Gyeonggi province (GRRCHanyang2020-B01), Hydrogen Energy Full Cycle Core Material Research Center), and a grant (GP2022-0012) from the Korea Research Institute of Standards and Science.

REFERENCES

- (1) Kunjachan, S.; Ehling, J.; Storm, G.; Kiessling, F.; Lammers, T. *Chem. Rev.* **2015**, *115*, 10907–10937.
- (2) Lilly Thankamony, A. S.; Wittmann, J. J.; Kaushik, M.; Corzilius, B. *Prog. Nucl. Magn. Reson. Spectrosc.* **2017**, *102–103*, 120–195.
- (3) Jannin, S.; Dumez, J.-N.; Giraudeau, P.; Kurzbach, D. *J. Magn. Reson.* **2019**, *305*, 41–50.
- (4) Sun, X.; Cai, Y.; Xu, Z.; Zhu, D. *Molecules* **2019**, *24*, 1477.
- (5) Sun, C.; Fang, C.; Stephen, Z.; Veiseh, O.; Hansen, S.; Lee, D.; Ellenbogen, R. G.; Olson, J.; Zhang, M. *Nanomedicine* **2008**, *3*, 495–505.
- (6) Davis, M. E.; Chen, Z.; Shin, D. M. *Nat. Rev. Drug Discovery* **2008**, *7*, 771–782.
- (7) Yao, Y.; Zhao, D.; Li, N.; Shen, F.; Machuki, J. O.; Yang, D.; Li, J.; Tang, D.; Yu, Y.; Tian, J.; Dong, H.; Gao, F. *Anal. Chem.* **2019**, *91*, 7850–7857.
- (8) Shi, D.; Si, Z.; Xu, Z.; Cheng, Y.; Lin, Q.; Fu, Z.; Fu, W.; Yang, T.; Shi, H.; Cheng, D. *Anal. Chem.* **2022**, *94*, 3819–3830.
- (9) Rotz, M. W.; Culver, K. S. B.; Parigi, G.; MacRenaris, K. W.; Luchinat, C.; Odom, T. W.; Meade, T. J. *ACS Nano* **2015**, *9*, 3385–3396.
- (10) Shao, C.; Li, S.; Gu, W.; Gong, N.; Zhang, J.; Chen, N.; Shi, X.; Ye, L. *Anal. Chem.* **2015**, *87*, 6251–6257.
- (11) Zhang, L.; Liu, Y.; Zhang, Q.; Li, T.; Yang, M.; Yao, Q.; Xie, X.; Hu, H.-Y. *Anal. Chem.* **2018**, *90*, 1934–1940.
- (12) Li, Y.; Zhang, H.; Guo, C.; Hu, G.; Wang, L. *Anal. Chem.* **2020**, *92*, 11739–11746.
- (13) Björgvinsdóttir, S.; Emsley, L. *Chimia* **2021**, *75*, 333.
- (14) Lee, Y. *Appl. Spectrosc. Rev.* **2016**, *51*, 210–226.
- (15) Mishra, A.; Pariani, G.; Oerther, T.; Schwaiger, M.; Westmeyer, G. G. *Anal. Chem.* **2016**, *88*, 10790–10794.
- (16) Rayner, P. J.; Richardson, P. M.; Duckett, S. B. *Angew. Chem., Int. Ed.* **2020**, *59*, 2710–2714.
- (17) Whiting, N.; Hu, J.; Zacharias, N. M.; Lokesh, G. L. R.; Volk, D. E.; Menter, D. G.; Rupaimoole, R.; Previs, R.; Sood, A. K.; Bhattacharya, P. *J. Med. Imag.* **2016**, *3*, 036001.
- (18) Ardenkjaer-Larsen, J. H.; Fridlund, B.; Gram, A.; Hansson, G.; Hansson, L.; Lerche, M. H.; Servin, R.; Thaning, M.; Golman, K. *Proc. Natl. Acad. Sci. U.S.A.* **2003**, *100*, 10158–10163.
- (19) Smith, A. N.; Märker, K.; Hediger, S.; De Paëpe, G. *J. Phys. Chem. Lett.* **2019**, *10*, 4652–4662.
- (20) Dementyev, A. E.; Cory, D. G.; Ramanathan, C. *Phys. Rev. Lett.* **2008**, *100*, 127601.
- (21) Cassidy, M. C.; Chan, H. R.; Ross, B. D.; Bhattacharya, P. K.; Marcus, C. M. *Nat. Nanotechnol.* **2013**, *8*, 363–368.
- (22) Atkins, T. M.; Cassidy, M. C.; Lee, M.; Ganguly, S.; Marcus, C. M.; Kauzlarich, S. M. *ACS Nano* **2013**, *7*, 1609–1617.
- (23) Whiting, N.; Hu, J.; Shah, J. V.; Cassidy, M. C.; Cressman, E.; Zacharias Millward, N.; Menter, D. G.; Marcus, C. M.; Bhattacharya, P. *K. Sci. Rep.* **2015**, *5*, 12842.
- (24) Aptekar, J. W.; Cassidy, M. C.; Johnson, A. C.; Barton, R. A.; Lee, M.; Ogier, A. C.; Vo, C.; Anahtar, M. N.; Ren, Y.; Bhatia, S. N.; Ramanathan, C.; Cory, D. G.; Hill, A. L.; Mair, R. W.; Rosen, M. S.; Walsworth, R. L.; Marcus, C. M. *ACS Nano* **2009**, *3*, 4003–4008.
- (25) Seo, H.; Choi, I.; Whiting, N.; Hu, J.; Luu, Q. S.; Pudakalakatti, S.; McCowan, C.; Kim, Y.; Zacharias, N.; Lee, S.; Bhattacharya, P.; Lee, Y. *ChemPhysChem* **2018**, *19*, 2143–2147.
- (26) Kwiatkowski, G.; Polyhach, Y.; Jähnig, F.; Shiroka, T.; Starsich, F. H. L.; Ernst, M.; Kozerke, S. *J. Phys. Chem. C* **2018**, *122*, 25668–25680.
- (27) Hu, J.; Whiting, N.; Bhattacharya, P. *J. Phys. Chem. C* **2018**, *122*, 10575–10581.
- (28) Pudakalakatti, S.; Enriquez, J. S.; McCowan, C.; Ramezani, S.; Davis, J. S.; Zacharias, N. M.; Bourgeois, D.; Constantinou, P. E.; Harrington, D. A.; Carson, D.; Farach-Carson, M. C.; Bhattacharya, P. *K. Wiley Interdiscip. Rev.: Nanomed. Nanobiotechnol.* **2021**, *13*, No. e1722.
- (29) Kim, J.; Jo, D.; Yang, S.-H.; Joo, C.-G.; Whiting, N.; Pudakalakatti, S.; Seo, H.; Son, H. Y.; Min, S.-J.; Bhattacharya, P.; Huh, Y.-M.; Shim, J. H.; Lee, Y. *ACS Appl. Mater. Interfaces* **2021**, *13*, 56923–56930.
- (30) Cassidy, M. C.; Ramanathan, C.; Cory, D. G.; Ager, J. W.; Marcus, C. M. *Phys. Rev. B: Condens. Matter Mater. Phys.* **2013**, *87*, 161306.
- (31) Thomassen, L. C. J.; Aerts, A.; Rabolli, V.; Lison, D.; Gonzalez, L.; Kirsch-Volders, M.; Napierska, D.; Hoet, P. H.; Kirschhock, C. E. A.; Martens, J. A. *Langmuir* **2010**, *26*, 328–335.
- (32) Quan, B.; Lee, C.; Yoo, J. S.; Piao, Y. *J. Mater. Chem. B* **2017**, *5*, 586–594.
- (33) Zhang, Y.; Peng, J.; Liu, Z.; Zou, H.; Wu, R. *Anal. Chem.* **2016**, *88*, 8380–8384.
- (34) Peng, J.; Li, J.; Xu, W.; Wang, L.; Su, D.; Teoh, C. L.; Chang, Y.-T. *Anal. Chem.* **2018**, *90*, 1628–1634.
- (35) Myers, S. A.; Cygan, R. T.; Assink, R. A.; Boslough, M. B. *Phys. Chem. Miner.* **1998**, *25*, 313–317.
- (36) Malfait, W. J.; Halter, W. E.; Verel, R. *Chem. Geol.* **2008**, *256*, 269–277.
- (37) Chemtob, S. M.; Rossman, G. R.; Stebbins, J. F. *Am. Mineral.* **2012**, *97*, 203–211.
- (38) Lafon, O.; Rosay, M.; Aussenac, F.; Lu, X.; Trébosc, J.; Cristini, O.; Kinowski, C.; Touati, N.; Vezin, H.; Amoureux, J.-P. *Angew. Chem., Int. Ed.* **2011**, *50*, 8367–8370.
- (39) Valla, M.; Rossini, A. J.; Caillot, M.; Chizallet, C.; Raybaud, P.; Digne, M.; Chaumonnot, A.; Lesage, A.; Emsley, L.; van Bokhoven, J. A.; Copéret, C. *J. Am. Chem. Soc.* **2015**, *137*, 10710–10719.
- (40) Rossini, A. J.; Zagdoun, A.; Lelli, M.; Gajan, D.; Rascón, F.; Rosay, M.; Maas, W. E.; Copéret, C.; Lesage, A.; Emsley, L. *Chem. Sci.* **2012**, *3*, 108–115.
- (41) Gajan, D.; Schwarzwälder, M.; Conley, M. P.; Grüning, W. R.; Rossini, A. J.; Zagdoun, A.; Lelli, M.; Yulikov, M.; Jeschke, G.; Sauvée, C.; Ouari, O.; Tordo, P.; Veyre, L.; Lesage, A.; Thieuleux, C.; Emsley, L.; Copéret, C. *J. Am. Chem. Soc.* **2013**, *135*, 15459–15466.
- (42) Lelli, M.; Gajan, D.; Lesage, A.; Caporini, M. A.; Vitzthum, V.; Miéville, P.; Héroguel, F.; Rascón, F.; Roussey, A.; Thieuleux, C.; Boualleg, M.; Veyre, L.; Bodenhausen, G.; Coperet, C.; Emsley, L. *J. Am. Chem. Soc.* **2011**, *133*, 2104–2107.
- (43) Yokoi, T.; Sakamoto, Y.; Terasaki, O.; Kubota, Y.; Okubo, T.; Tatsumi, T. *J. Am. Chem. Soc.* **2006**, *128*, 13664–13665.
- (44) Kim, H. S.; Lee, C. H.; Jang, J.-H.; Kang, M. S.; Jin, H.; Lee, K.-S.; Lee, S. U.; Yoo, S. J.; Yoo, W. C. *J. Mater. Chem. A* **2021**, *9*, 4297–4309.
- (45) Cho, K. G.; Kim, H. S.; Jang, S. S.; Kyung, H.; Kang, M. S.; Lee, K. H.; Yoo, W. C. *Adv. Funct. Mater.* **2020**, *30*, 2002053.
- (46) Akbey, U.; Altin, B.; Linden, A.; Özçelik, S.; Gradzielski, M.; Oschkinat, H. *Phys. Chem. Chem. Phys.* **2013**, *15*, 20706–20716.

(47) Nilsson, E. J.; Huber, M.; Carlström, G.; Söderman, O.; Bowron, D. T.; Edler, K. J.; Alfredsson, V. *Phys. Chem. Chem. Phys.* **2019**, *21*, 6732–6742.

(48) Pilgrim, C. D.; Colla, C. A.; Ochoa, G.; Walton, J. H.; Casey, W. H. *Commun. Chem.* **2018**, *1*, 67.

Recommended by ACS

Modern Manufacturing Enables Magnetic Field Cycling Experiments and Parahydrogen-Induced Hyperpolarization with a Benchtop NMR

Frowin Ellermann, Andrey N. Pravdivtsev, *et al.*

APRIL 05, 2023

ANALYTICAL CHEMISTRY

READ 

Competitive Displacement Restores the Hyperpolarized ^{15}N NMR Signal in Blood Plasma

Eul H. Suh and Zoltan Kovacs

DECEMBER 19, 2022

ACS PHYSICAL CHEMISTRY AU

READ 

Diffusion NMR for Measuring Dynamic Ligand Exchange on Colloidal Nanocrystals

Xiaoqi Zhou, Xueqian Kong, *et al.*

DECEMBER 15, 2022

ANALYTICAL CHEMISTRY

READ 

Coordination-Driven Self-Assembly of Iron Oxide Nanoparticles for Tumor Microenvironment-Responsive Magnetic Resonance Imaging

Jinhong Hou, Leyu Wang, *et al.*

NOVEMBER 03, 2022

ANALYTICAL CHEMISTRY

READ 

Get More Suggestions >